DBSproc: An Open Source Process for DBS Electrode Localization and Tractographic Analysis

Peter M. Lauro,[1] Nora Vanegas-Arroyave,[1,2] Ling Huang,[1] Paul A. Taylor,[3,4] Kareem A. Zaghloul,[5] Codrin Lungu,[1] Ziad S. Saad,[6] and Silvina G. Horovitz[2]*

[1]*Office of the Clinical Director, National Institute of Neurological Disorders and Stroke, National Institutes of Health, Bethesda, Maryland*
[2]*Human Motor Control Section, National Institute of Neurological Disorders and Stroke, National Institutes of Health, Bethesda, Maryland*
[3]*Department of Human Biology, Faculty of Health Sciences, University of Cape Town, MRC/UCT Medical Imaging Research Unit, Cape Town, South Africa*
[4]*African Institute for Mathematical Sciences, Muizenberg, Western Cape, South Africa*
[5]*Surgical Neurology Branch, National Institute of Neurological Disorders and Stroke, National Institutes of Health, Bethesda, Maryland*
[6]*Statistical and Scientific Computing Core, National Institute of Mental Health, National Institutes of Health, Bethesda, Maryland*

◆━━━━━━━━━━━━━━━━━━━━━━━━━━◆

Abstract: Deep brain stimulation (DBS) is an effective surgical treatment for movement disorders. Although stimulation sites for movement disorders such as Parkinson's disease are established, the therapeutic mechanisms of DBS remain controversial. Recent research suggests that specific white-matter tract and circuit activation mediates symptom relief. To investigate these questions, we have developed a patient-specific open-source software pipeline called 'DBSproc' for (1) localizing DBS electrodes and contacts from postoperative CT images, (2) processing structural and diffusion MRI data, (3) registering all images to a common space, (4) estimating DBS activation volume from patient-specific voltage and impedance, and (5) understanding the DBS contact-brain connectivity through probabilistic tractography. In this paper, we explain our methodology and provide validation with anatomical and tractographic data. This method can be used to help investigate mechanisms of action of DBS, inform surgical and clinical assessments, and define new therapeutic targets. *Hum Brain Mapp 37:422–433, 2016.* Published 2015. This article is a U.S. Government work and is in the public domain in the USA.

Key words: magnetic resonance imaging (MRI); neurostimulation; deep brain stimulation (DBS); diffusion tensor imaging (DTI); Parkinson's disease (PD)

◆━━━━━━━━━━━━━━━━━━━━━━━━━━◆

INTRODUCTION

Deep brain stimulation (DBS) is an established, effective surgical treatment for movement disorders, and it is increasingly employed for other indications. DBS allows for adjustable and reversible modulation of neural networks. Although stimulation sites for disorders such as Parkinson's disease (PD), dystonia, and essential tremor are well established, their therapeutic mechanisms are still a matter of debate and controversy [Hubble et al., 1996; Limousin et al., 1998; Vidailhet et al., 2005].

Recent research has posited that DBS relieves symptoms by the selective stimulation of white-matter tracts [Henderson, 2012] or by the normalization of pathologic global functional networks [Kringelbach et al., 2011]. Noninvasive *in vivo* MRI characterization of structural connectivity is currently accomplished with diffusion weighted imaging (DWI) techniques, such as diffusion tensor imaging (DTI). As myelinated axons differentially constrain diffusion of water molecules along their axes, DTI provides a good estimate of white-matter location and principal orientation [Basser and Pierpaoli, 1996]. Although not necessarily an accurate anatomical measure [Thomas et al., 2014], DTI-based tractography nevertheless has been shown to identify certain continuous paths, and changes to those paths, throughout diffusion MR datasets [Jones et al., 2013].

Case studies characterizing optimal DBS targets using DTI have isolated specific relevant white-matter targets [Anthofer et al., 2015; Kovanlikaya et al., 2014; Riva-Posse et al., 2014; Schlaier et al., 2015; Sweet et al., 2014]. However, these studies have been limited to small sample sizes, and tractography measures have been based on deterministic rather than probabilistic tractography, whereas the latter has been demonstrated to provide more robust estimates of underlying white-matter structures [Descoteaux et al., 2009]. In addition, these studies have typically used proprietary software that obstructs replication and comparisons across centers and studies.

A major limitation in the field is the proper coregistration of contacts into the presurgical image space, where diffusion data is collected. There is currently no gold standard for this coregistration, and the set of contact coordinates defined for surgery are referenced to landmarks manually defined within proprietary software (see Supporting Information). Thus, it is sometimes not practical to translate contact coordinates into the space where the DTI data is analyzed.

To address these issues, we present a scalable, modular, and open-source software pipeline called 'DBSproc' for merging preoperative T1-, T2-, and diffusion-weighted (T1w, T2w, and DW) MR images with postoperative T1w MR and CT images for accurate DBS electrode localization and tractographic analysis. Our pipeline includes specifically tailored scripting and runs alongside several specialized, publically available software packages, such as: FreeSurfer, for white- and grey-matter segmentation [Fischl, 2012; http://surfer.nmr.mgh.harvard.edu]; Medical Image Processing, Analyzing and Visualization (MIPAV), for AC–PC alignment [Bazin et al., 2007; McAuliffe et al., 2001; http://mipav.cit.nih.gov]; TORTOISE, for diffusion image preprocessing [Pierpaoli et al., 2010; http://science.nichd.nih.gov/confluence/display/nihpd/TORTOISE]; AFNI, for MR/CT image registration; SUMA, for 3D surface manipulation; and FATCAT, for DTI and probabilistic tractography estimation [Cox, 1996; Saad and Reynolds, 2012; Taylor and Saad, 2013; http://afni.nimh.nih.gov]. The presented pipeline, included now in the AFNI distribution, can be executed via two scripts, and it allows for patient-specific localization and tractographic analysis, regardless of DBS implantation site. Our processing brings all the data to the same space, where diffusion tractography is estimated from the automatically detected DBS contacts. In this paper, we explain the methodology, provide instructions for accessing scripts and sample data, and provide initial validation with data within a PD DBS population.

MATERIALS AND METHODS

Patient Population

We analyzed imaging data from twenty-six patients (12 females, age: 56.9 ± 9.75 years) with idiopathic PD who received bilateral subthalamic nucleus (STN) (22 patients; 11 females, age: 57.4 ± 9.17 years) or globus pallidus pars interna (GPi) (4 patients; 1 female, age: 54.3 ± 13.9 years) DBS surgery at the National Institutes of Health (NIH) from 2011 to 2014. This study was conducted in accordance with NIH Institutional Review Board-approved protocols, and informed consent was obtained from all patients. Patients were diagnosed with PD in accordance with the UK Parkinson's Disease Society Brain Bank Clinical Diagnostic Criteria [Hughes et al., 1992]. All procedures followed approved standard of care.

Surgical Procedure and Follow-up

All patients received pre- and postoperative MRI and CT scans, described in detail in the next section. The surgical target was localized anatomically on preoperative imaging (coregistered T1w, T2w, and CT images using StealthStation i7, Medtronic, Minneapolis, MN) combined with intraoperative microelectrode recordings. All patients were implanted with DBS Lead Model 3389 (each lead/electrode has four 1.5 mm contacts, with gaps of 0.5 mm, Medtronic).

One month after DBS implantation the patients underwent screening of each contact, where an experienced movement disorder neurologist determined the presence of clinical benefits on the dominant, relevant cardinal symptoms for each patient, as well as the presence of immediate side effects [Volkmann et al., 2006]. The therapeutic benefit of neurostimulation is defined to be the observed improvement in any of the cardinal symptoms of PD (tremor, bradykinesia, and rigidity) in the absence of side effects. Side effects might include motor contractions, sensory,

emotional, and vision changes, depending on the contact location and stimulating parameters.

During the screening session, the voltage thresholds for clinical benefits (*entry voltage*) and for side effects (*exit voltage*) were determined for each contact. The difference between *exit* and *entry* voltages determined the *therapeutic window* of each contact. For each patient and each hemisphere, we defined the *selected contact* (SC) to be the one with the greatest therapeutic window.

Contacts that caused only side effects (i.e., that have a therapeutic window of 0V) at voltages below the averaged SC hemispheric entry voltage were labeled as *noneffective* (NE) contacts. Impedances provided by the DBS programming unit were recorded for the SC at the chronic stimulation voltage, and these are shown in Supporting Information Table I.

Image Acquisition

Preoperative MRI included T1w, T2w, and DW images collected at 3.0 T. Postoperative MRI consisted of T1w images collected at 1.5 T. Both pre- and postoperative CT images were acquired on the same multidetector scanner.

Preoperative MRI was acquired on a 3.0 T scanner (Philips Achieva XT, Philips Medical Systems, Best, The Netherlands) with an 8-channel sensitivity encoded head coil (SENSE, Philips). MRI data comprises a three-dimensional T1w turbo-field-echo, a T2w turbo-spin-echo, and a DW high-angle echo-planar imaging (EPI) sequence.

The T1w turbo-field-echo sequence was acquired with the following parameters: TR: 8.15 ms, TE: 3.735 ms, slice thickness: 1.00 mm, spacing between slices: 1.00 mm, echo train length: 240, FOV: 240 × 240 mm^2 (inplane resolution 0.9375 × 0.9375 mm^2), flip angle: 8°, acquisition matrix: 240 × 240 interpolated to 256 × 256 with 191 sagittal locations, and total acquisition time: 6 min and 53 s. The T2w turbo-spin-echo sequence was acquired with the following parameters: TR: 2500 ms, TE: 235.648 ms, slice thickness: 1.10 mm, spacing between slices: 0.55 mm, echo train length: 133, FOV: 250 × 250 mm^2 (inplane resolution 0.9765 × 0.9765 mm^2), flip angle: 90°, acquisition matrix: 228 × 226, interpolated to 256 × 256 with 327 sagittal locations, and total acquisition time: 4 min and 37.5 s. Finally, the DW high-angle EPI sequence was acquired with the following parameters: TR: 9776.51 ms, TE: 65 ms, slice thickness: 2.00 mm, spacing between slices: 2.00 mm, echo train length: 59, FOV: 224 × 224 mm^2 (inplane resolution 2.0 × 2.0 mm^2), flip angle: 90°, acquisition matrix: 112 × 112 with 78 axial locations, 1 reference b_0 volume, 33 noncollinear gradient directions with $b = 1000$ s/mm^2, and total acquisition time: 6 min and 48 s.

Postoperative clinical MRI was acquired on a 1.5 T scanner (Philips Achieva XT) with an H-Head Coil (Philips). A three-dimensional T1w fast-field-echo sequence was acquired with the following parameters: TR: 9.95 ms, TE: 4.524 ms, slice thickness: 1.00 mm, spacing between slices: 1.00 mm, echo train length: 1, FOV: 240 × 240 mm^2 (inplane resolution 0.9375 × 0.9375 mm), flip angle: 15°, acquisition matrix: 240 × 240 interpolated to 256 × 256 with 171 sagittal locations, and total acquisition time: 6 min and 48 s. The SAR for all postoperative scans was kept below 0.1 W/kg body weight, in accordance with Medtronic MRI safety parameters.

Pre- and postoperative CT scans were acquired on a multidetector scanner (Siemens SOMATOM Definition Flash, Siemens Healthcare, Erlangen, Germany). CT scans were acquired with the following parameters: tube voltage: 120 kV, tube current: 239 mA, data collection diameter: 500 mm, reconstruction diameter: 250 mm, acquisition matrix: 512 × 512 with 210 axial locations, slice thickness: 1.00 mm, pixel spacing: 0.4883 × 0.4883 mm.

Image Processing

All MR and CT DICOM images were reconstructed to nifti volumes using the 'dcm2nii' command from the MRIcron software package [Rorden and Brett, 2000; http://www.mccauslandcenter.sc.edu/mricro/mricron]. T2w data is aligned in MIPAV and DW images are preprocessed in TORTOISE (see "Preprocessing"). Image registration and tractography are performed within DBSproc, executable with two scripts: @DBSproc1 (see "Images preparation: @DBSproc1") and @DBSproc2 (see "Contact reconstruction and probabilistic tractography: @DBSproc2"). These two novel scripts are now part of the AFNI distribution and can be manually installed, together with a sample dataset, by running the command @Install_DBSproc. Here we provide an outline of image-specific processing and registration; see Figure 1 for a schematic of the pipeline, detailing steps performed in each script. Additional information for each step is included as Supporting Information: DBSproc Documentation. Finally, we provide several validation strategies (see "Validation").

Preprocessing

Preoperative T2w

Anterior and posterior commissure (AC and PC) landmarks were manually defined on the preoperative T2w volume using MIPAV software package. A rigid body transform was then applied resulting in a horizontal AC–PC line and a vertical midsagittal plane. The transformed volume was visually inspected.

Diffusion weighted images

DWIs were used to estimate diffusion tensors and maps of their associated DTI parameters, such as the principal directions of diffusion, eigenvalues, fractional anisotropy (FA), and mean diffusivity, which were used to quantitatively compare brain tissue properties. FA and principal diffusion directions were used for estimating white-matter fiber trajectories, and their confidence intervals were calculated for the implementation of probabilistic tractography (see "FATCAT and tractography estimation").
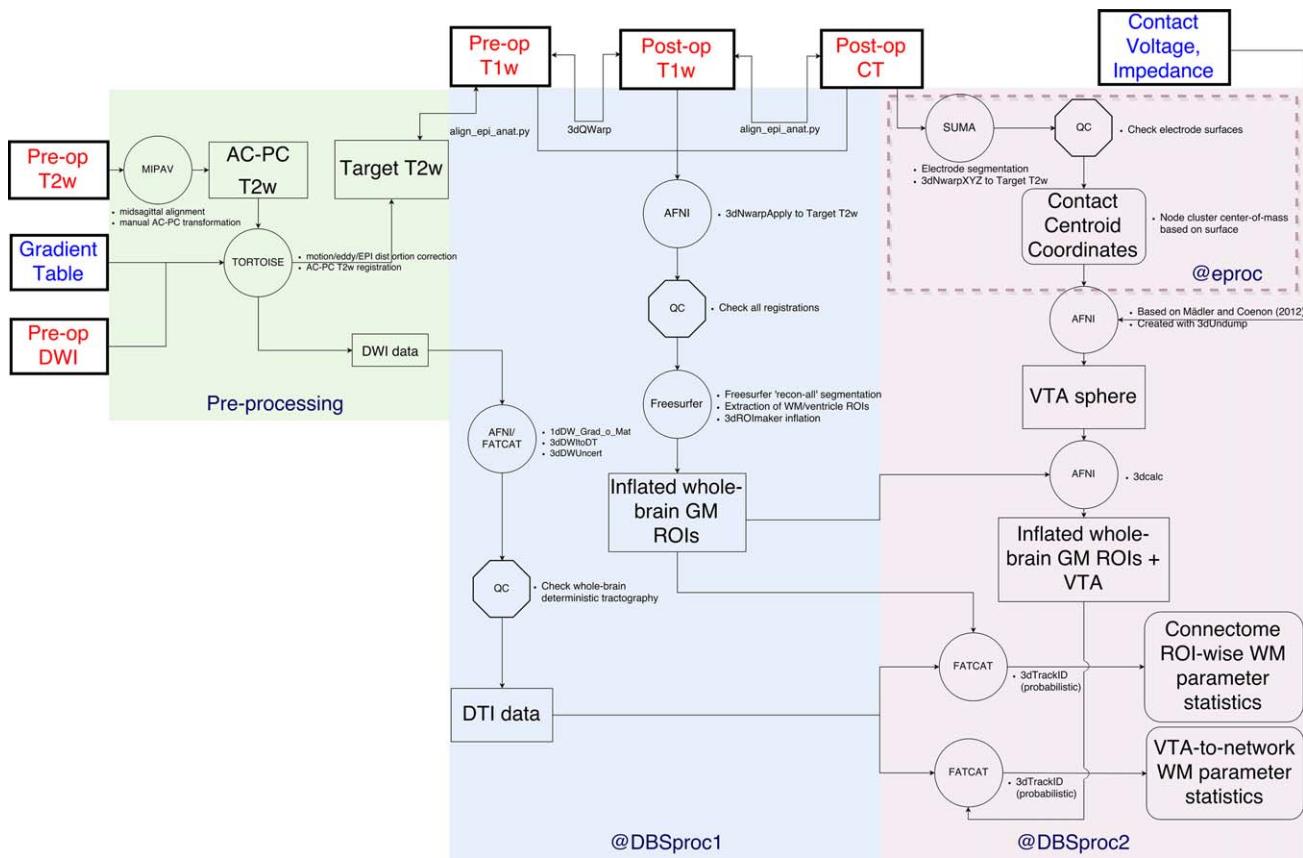
Figure 1.

Flowchart illustrating the processing pipeline. Preprocessing, @DBSproc1 and @DBSproc2 (including @eproc, indicated by the dashed box) are indicated in colored boxes with their individual steps inside. Bold boxes represent input data. Red text represents images in original space, and blue text represents nonimaging input data. Rectangles with black text represent intermediate data in target T2w space, circles indicate software used, and octagons repre- sent quality-check points, and rounded rectangles indicate output data. Specific functions/steps are annotated next to shapes. T1w/T2w = T1/T2-weighted images, DWI = diffusion weighted images, DTI = diffusion tensor imaging, AC–PC = anterior/ posterior commissure-marked, GM = grey matter, ROIs = regions of interest, VTA = volume of tissue activated, WM = white matter, QC = quality check.

In TORTOISE, diffusion imaging volumes were motion-, eddy-, and EPI distortion-corrected, coregistered to the AC–PC aligned T2w volume, and resampled to 1.5 mm isotropic voxels using standard settings in the 'DIFF_ PREP' tool. FA and directionally encoded color (DEC) data were subsequently computed using 'DIFF_CALC', and resultant datasets were visually quality checked and exported to nifti format using the 'export images', then 'AFNI' option. The TORTOISE-processed T2w volume was also exported, and this served as the registration target for diffusion data and all other volumes (henceforth referred to as the target T2w volume).

Images Preparation: @DBSproc1

This script reads the output from TORTOISE, the preop- erative T1w, and the postoperative T1w and CT images,

and prepares the data for tractography. It includes tissue segmentation, image registration and DTI calculations.

Tissue segmentation and ROI setup

Reconstructed T1w image was intensity-normalized using AFNI's '3dUnifize' and skull-stripped using the FreeSurfer command 'recon-all' up to the '–normalization2' option. The skull-stripped T1w volume was affinely registered to the target T2w volume using AFNI's 'align_epi_anat.py' with the local Pearson's coefficient (LPC) cost function [Saad et al., 2009]. The registered T1w volume was fed back into FreeSurfer for generating cortical surface models and parcel- lations, such as 'aparc + aseg' via the 'recon-all' command with no additional skull stripping ('−noskullstrip' option). FreeSurfer-generated volumes and surfaces were imported into SUMA using the '@SUMA_Make_Spec_FS' script. The

processed, preoperative T1w structural image was used to create grey-matter (GM) regions of interest (ROIs) as target ROIs for tractography. Specifically, the ROIs were dilated with '3dROIMaker' by a maximum of two neighboring voxel layers with the '-neigh_face_edge' option that defines two voxels sharing a face or an edge to be neighbors. The expansion was stopped if it reached either another ROI (preventing ROI overlap) or voxels with an FA value larger than 0.2 (preventing white-matter overrun).

Image alignments

A custom AFNI script performed an affine registration of each patient's postoperative CT and T1w volumes, an affine registration of each patient's preoperative T1w and target T2w volumes, and a nonlinear registration of each patient's pre- and postoperative T1w volumes. All volume registrations were visually checked for quality. From the calculated transformations, all images were registered to the target T2w volume, as DWIs had been registered to this space during TORTOISE preprocessing.

Postop CT –> Postop T1w. To prepare the postoperative T1w volume for registration to the postoperative CT volume, low-signal regions were masked using AFNI's '3dAutomask', followed by an intensity inversion. After centering the CT image to the postoperative T1w, a brain tissue mask was created from the postoperative CT using the intensity value range for soft tissue from the Hounsfield scale [Hebb and Poliakov, 2009]. The postoperative CT tissue mask and inverted T1w volume were then centered and affinely registered at the lower resolution of the T1w volume using AFNI's 'align_epi_anat.py' with the normalized Mutual Information cost function [Wells et al., 1996]. Registration was verified using electrode trajectories in each image (hypointensities in the T1w, hyperintensities in the CT) as quality control [Paek et al., 2008; Pinsker et al., 2008].

Preop T1w –> Target T2w. Skull-stripped preoperative T1w volume was affinely registered to skull-stripped target T2w volume using AFNI's 'align_epi_anat.py' with the LPC cost function.

Postop T1w –> Preop T1w. Pre- and postoperative skull-stripped T1w volumes underwent nonlinear registration with AFNI's '3dQwarp'.

Transformation concatenation. After manually quality checking all three registrations, transformation matrices and displacement volumes computed in section "Image alignments" were concatenated to bring each of the original volumes into registration with the target T2w volume in one step to minimize blurring from sequential resampling.

DWI data preprocessing and DTI estimation

Gradient direction data obtained from DWI DICOM images was AFNI-formatted using AFNI's '1dDW_Gra-d_o_Mat' with scanner-specific formatting (e.g., averaging $b = 0$ references and matching scanner and file header coordinate frames). After TORTOISE preprocessing, tensors were estimated from diffusion data using AFNI's '3dDWItoDT' using nonlinear fits. As a viewable quality control of TORTOISE preprocessing and the gradient matching, whole brain deterministic tractography was implemented using the FATCAT command '3dTrackID' with the 'DET' mode option. For this, default tracking parameters were used (FA >0.2, turning angle <60°, and keeping tracts with length >20 mm) to find tracts within the whole brain mask with OR logic. The resulting file was viewed in SUMA along with a volume image to ensure that no obvious regions had been masked out and that major bundles appeared where expected. Uncertainty intervals of FA and principal diffusion directions were estimated with '3dDWUncert' using 500 jackknife-resampling iterations, for use in the probabilistic tractography (see "FATCAT probabilistic tractography").

Contact Reconstruction and Probabilistic Tractography: @DBSproc2

DBS electrode/contact reconstruction and localization (@eproc within @DBSproc2)

Electrodes and contacts were automatically segmented and labeled from the postoperative CT volume by exaggerating the contrast of bright structures that were surrounded by darker tissue on the scale of 2 mm. Specifically, these steps isolated high intensity voxel clusters, selected voxel clusters inside the skull, and identified electrodes based on their geometry.

The original CT volume was segmented into multiple classes, such as air, soft tissue, two bone types, and metal using maximum likelihood classification in a uniform mixture of a Gaussian model [Gopinath, 1998]. The model was initialized with intensity parameters from the Hounsfield scale. Voxels labeled as bone were extracted. The resultant volume was first eroded by three voxels, and then dilated by three voxels, in order to retain clusters while reducing the likelihood of having clusters bridged by narrow structures. Clusters smaller than 10,000 voxels were also eliminated. A two-manifold surface, initialized as a sphere, was then deformed to wrap around the remaining bone-labeled voxels. Voxels inside that surface were then identified as electrodes and twelve erosion steps were undertaken to remove the majority of superior skull bone voxels. The final, eroded volume was used to mask a transformed version of the original CT in order to enhance the spatial contrast between the electrodes and the rest of the brain per the following voxel-wise equation:

$$Y_v' = [(M_i - M_o)/M_o] \times Y_v \qquad (1)$$

where

Y_v is the intensity at voxel v in the CT volume in Hounsfield units,

M_i is the average voxel intensity within a 2 mm radius inner sphere (S_i) centered on v,

M_o is the average voxel intensity within a 5 mm radius outer sphere (S_o) centered on v, but excluding voxels in regions S_i,

Y'_v is the transformed intensity at voxel v in the CT volume.

Clusters of more than twenty bright ($Y'_v > 1,000.0$) voxels were retained, and features for each of them (e.g., average intensity, volume, and center of mass coordinates) were assembled in order to distinguish electrode clusters. The principal directions and eigenvalues of each cluster were then estimated, and were used to capture cluster shape with estimated surface anisotropy (SA, values range from 0 being isotropic sphere to 1 being one-dimensional rod) and linear measure (C_l) values. Note that SA, principal directions, and eigenvalues were calculated from each cluster's geometry, not from diffusion data. Cluster orientation was estimated as the dot product of the cluster's principal direction and the z axis, as electrodes were inserted from superior openings in the cranium. The two electrodes were identified as the largest two clusters having a mean intensity value larger than 1000, SA and C_l larger than 0.95, and a dot product larger than 0.5. Automatic identification of left and right electrodes was based on their centers of mass's x-coordinate (with the larger value corresponding to the left side). After successful electrode isolation, electrode volume masks and contour surface coordinates were also transformed into the target T2w space by concatenation of appropriate spatial transforms using AFNI's '3dNwarpXYZ'.

To assign depth along an electrode, a surface model of its cluster was constructed, and each node was projected along its computed principal direction. The bottommost node was identified, and subsequent node depth was determined based on the distance between a node's projection along the principal direction and that of the bottom node. To reduce effects of electrode surface curvature, nodes of depth up to 35 mm were included in the estimation of the principal direction. The four contacts of each electrode were identified by grouping nodes within depths ±1 mm of 2.25, 4.25, 6.25, and 8.25 mm defined from the electrode geometry. The centers of mass for these groups were computed and represented the centroid coordinates of the contacts to be used for constructing volumes of tissue activation detailed next.

Volume of tissue activated (VTA)

The volume of tissue activated (VTA) was estimated as a sphere centered at the contact centroid coordinate whose radius was calculated from individual therapeutic impedance and stimulation voltage, as described by the follow-

ing equation from the literature [Mädler and Coenen, 2012]:

$$r = -((k_4 \times I) - \sqrt{(k_4)^2 \times (I)^2 + 2 \times k_1 \times k_4 \times I + (k_1)^2 + 4 \times k_3 \times V}) + k_1)/(2 \times k_3) \qquad (2)$$

where

I is the electrode impedance in ohms, V is the contact voltage in volts,

k_4, k_1, and k_3 are model constants with values of 0.0009856, 21.0473, and 0.2786, respectively,
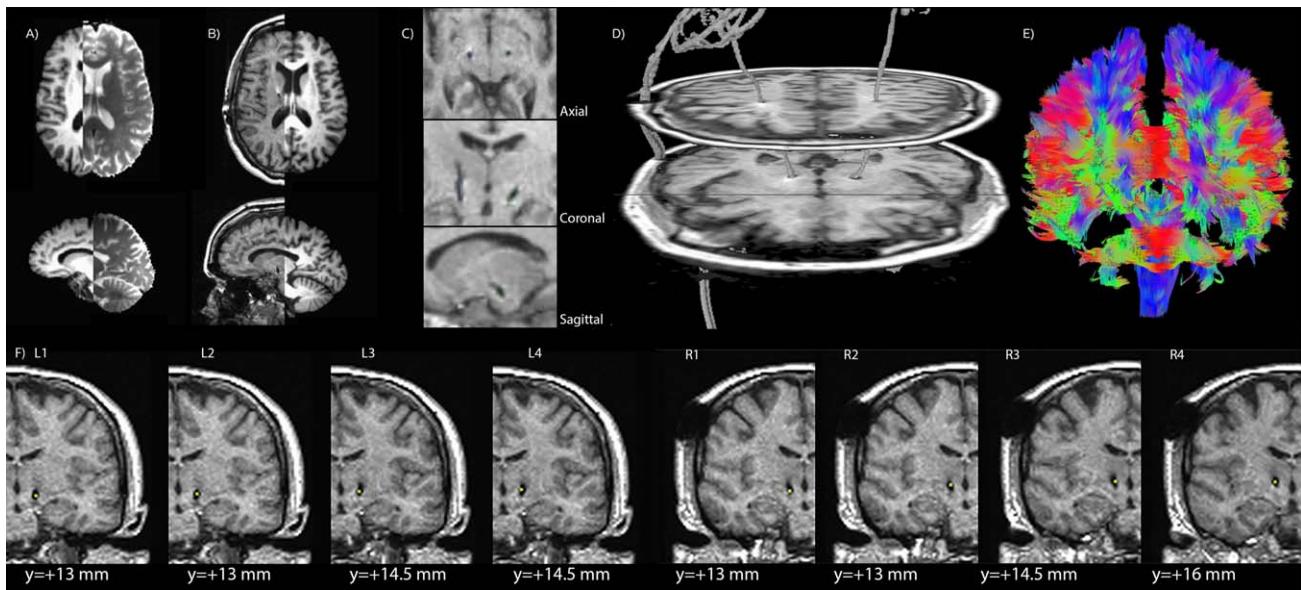
r is the calculated VTA sphere radius in millimeters.

Impedances and stimulation voltages are patient-dependent, thus this information is provided by the user as an input text file per hemisphere (l_volt.1D and r_volt.1D in the example dataset). Further information is provided in the Supporting Information: DBSproc Documentation.

FATCAT and tractography estimation

Network construction. For full probabilistic tractography, FATCAT uses repeated iterations of whole brain tracking to estimate the likelihood of structural WM connections between all pairs of target ROIs within a network. For this analysis, the network was composed by the 89 GM inflated ROIs (see "Tissue segmentation and ROI setup") with the addition of the VTA of interest. ROIs representing VTAs were added by replacing anatomical ROI values by the VTA ROI value (Supporting Information Fig. 1).

FATCAT probabilistic tractography. "Connectomic" probabilistic tractography on the whole brain GM parcellation was performed using the FATCAT command '3dTrackID' with the 'PROB' mode option. Tracking parameters used were: FA >0.2, turning angle <60°, keeping tracts with length >20 mm, thresholding fraction >0.021, five seeds per voxel and a total of 5000 Monte Carlo iterations [Taylor and Saad, 2013]. For each patient, connectomic connections were first calculated among the 89 inflated GM ROIs without any VTA, in order to understand the underlying intranetwork connectivity. To understand VTA-to-network connections, probabilistic tractography (with the same parameters as above) was then performed on the same set of anatomical ROIs plus the specific VTA ROI.

For connectomic data analysis, we examined the automatically generated '*.grid' file output of '3dTrackID', which contains matrices (here, of size 89 × 89) of output statistics describing the properties of the tractographic connections between all pairs of ROIs, such as the number of tracts and the mean and standard deviation of FA. For VTA-to-network data, we extracted a vector (1 × 90 '*.row' file) containing output statistics for the tractographic connections between the VTA and every other target ROI from the '*.grid' file using the FATCAT command 'fat_roi_row.py', specifying the VTA ROI value with the '−r' option.

Figure 2.

Images used for visually confirming registration quality. Image and coordinate data shown is from a single patient. (**A**) Preoperative T1w (left) and target T2w (right) volumes overlaid in the axial (top) and sagittal (bottom) planes. Volumes underwent an affine registration with AFNI's 'align_epi_anat.py'. (**B**) Post- (left) and preoperative (right) T1w volumes overlaid in the axial (top) and sagittal (bottom) planes. Volumes underwent a nonlinear registration in the AFNI function 'auto_warp.py'. (**C**) Postoperative T1w volume overlaid with green and blue outlines of the electrodes' surface reconstructed from registered CT images, zoomed-in views in axial, sagittal, and coronal. Volumes underwent an affine registration with AFNIs 'align_epi_anat.py'. (**D**) Reconstructed 3D surface of registered CT volume with two axial slices of postoperative T1w volume; electrodes shown as grey linear structures. (**E**) Anterior view of whole-brain deterministic tractography for quality control of processing, shown with properly formatted gradient direction data. (**F**) Yellow dots are eight contacts, as detected by DBSproc, for a single patient displayed on coronal views of postoperative T1w.

To visualize these tractographic network connections in SUMA, we performed a miniprobabilistic tractography, which is a methodology to include tensor uncertainty estimates with streamline tract propagation for increased robustness. The same default tracking parameters were utilized as previously described for deterministic tractography, except that we also performed 10 Monte Carlo iterations of tracking with perturbed tensor values, as a "mini" form of the full probabilistic tractography, while simultaneously maintaining a reasonable number of tracts for visualization [Taylor et al., 2015].
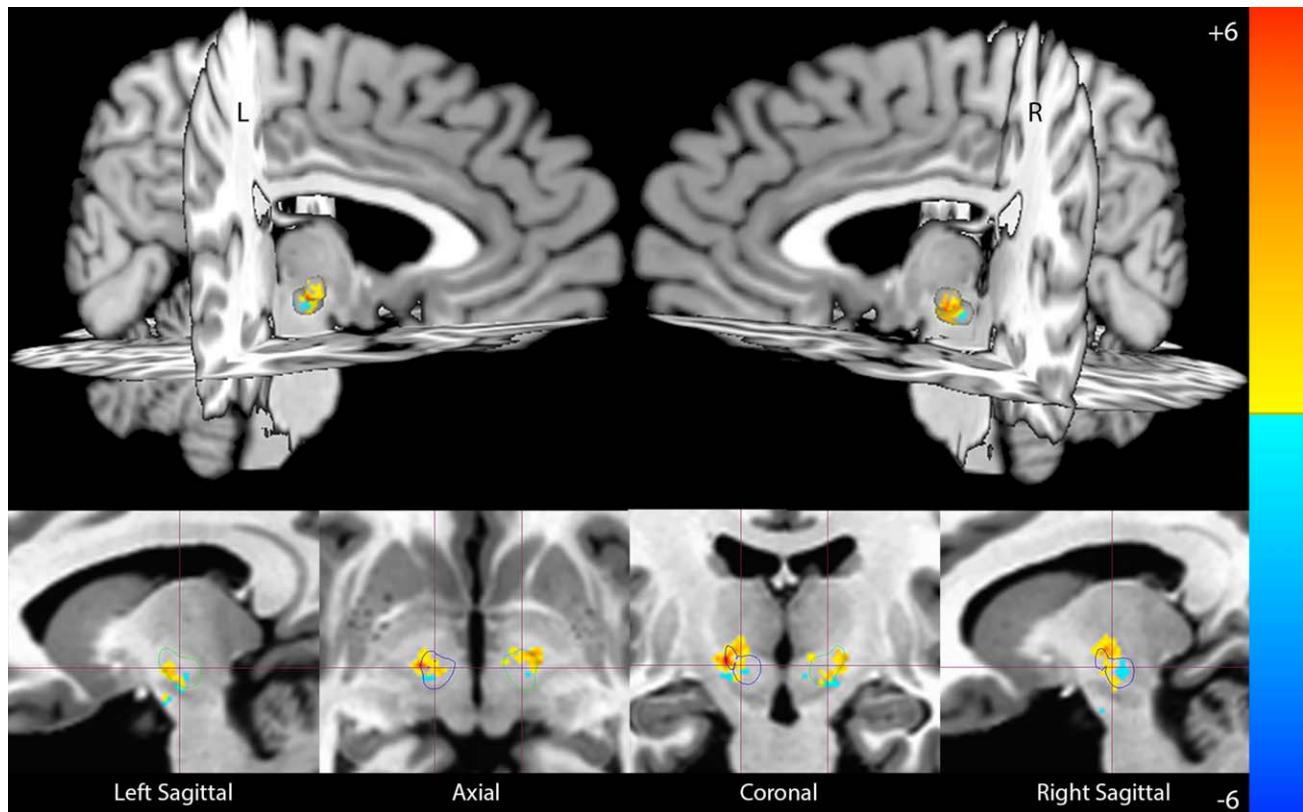
Validation

We have taken three steps to estimate the validity of our results beyond visual inspection of the registrations. First, we evaluated the contact location with respect to the STN. Second, we estimated the FA values for the selected VTAs and compared them to the average values of the STN. Third, we used the number of generated tracts as the proxy for a quality control measure for voltage adjustments (e.g., a wider WM area being covered when using a larger voltage).

Contact localization: anatomical validation

To compare contact coordinates among patients, we used the Talairach–Tournoux template ('TT space', the 1 mm isotropic AFNI volume 'TT_N27') as a common coordinate space. To do so, we used transformation matrices created from a nonlinear registration between each patient's target T2w-aligned preoperative T1w volume and TT_N27 using AFNI's '3dQwarp'. Spheres with a 2 mm radius centered at the contact centroid coordinate of each SC and NE were transformed to the TT space by applying the T1w-to-TT transformation matrix using AFNI's '3dNwarpApply'. We calculated the spatial distribution of the SCs (one per patient per hemisphere) and the NE contacts (those with no clinical benefits) with respect to the left and right STN ROIs in TT space.

Local fractional anisotropy estimation

To understand the structural properties of tissue surrounding contacts, we calculated average FA value and average size of our constructed VTAs. Specifically, we measured the

Figure 3.

Locations of stimulating contacts (SC) ($N = 22$ for each hemisphere) and noneffective contacts (NE) ($N = 7$ for left hemisphere, $N = 5$ for right hemisphere) represented as 2 mm spheres back-transformed back to standardized Talairach–Tournoux space (AFNI's TT_N27 volume) and overlaid on the 3D reconstructed TT_N27 STN ROIs (top). Bottom images show the same data in the TT_N27 sagittal, axial, and coronal plane (blue and green outlines represent STN ROIs' surfaces). Color bar represents the number of overlapping contacts: Yellow/red positive values represents SCs, blue negative values represent NE contacts.

FA values and the sizes of the VTAs created for the SCs at three voltage levels: 1 V, entry voltage and exit voltage. We also measured the FA values and sizes of VTAs created for the NE contacts at entry voltage. We normalized the distribution by its higher frequency value, to emphasize the shape of the distribution with respect to FA.
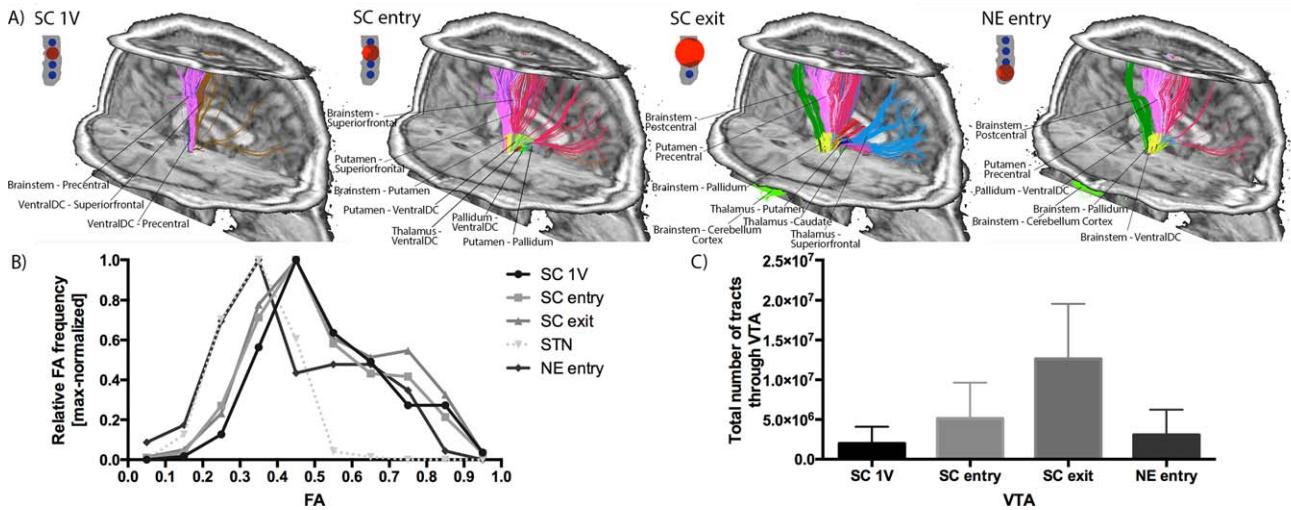
Finally, we measured the average FA value of each patient's STN, defined within the TT_N27 template, included in the AFNI distribution, and transformed to the patient space by applying the inverse T1w-to-TT transformation matrix, created in section "Contact localization: anatomical validation", using AFNI's '3dNwarpApply'. We note that, currently, there is no gold standard for the delineation of the STN. As a proxy for the demarcation, we inflated the STN ROIs. After this process, we calculated and compared the average values FA. A proper placement would be assumed to have a higher average FA when inflated, since the STN would be surrounded by fibers from the zona incerta, subthalamic fasciculus, ansa lenticularis, and internal capsule.

Tractography validation

To show how a change in contact voltage would affect tractography results between clinically relevant voltages, we compared the total number of VTA-to-network tracts from each patient's VTAs by performing an univariate general linear model analysis with voltage level (1 V, entry voltage, and exit voltage) as fixed effect, and with patient ID and contact label as random effects. Post hoc group comparisons were made with Bonferroni-corrected paired t tests. The total number of VTA-to-network tracts for NE contacts was compared to the corresponding hemisphere SC at entry voltage using a paired t test. Statistical analyses were performed with the SPSS software package (Version 19, IBM, Armonk, NY).

RESULTS

Registration results at each step (Fig. 2A–D) were visually inspected. The pipeline was observed to succeed for

Figure 4.

Volume of tissue activated (VTA) effects on tractography. Data shown at 1V, entry voltage, and exit voltage for the SCs and at entry voltage for NE contacts. (**A**) Single subject example of the tracts that VTA stimulates on a right hemisphere. SUMA images illustrate miniprobabilistic tract representations at selected stimulation voltages. In each case, the same image with miniprobabilistic tracts is shown passing through the given red sphere (represents VTA). Bundles of tract connections between two particular GM ROIs that pass by VTA are indicated in different colors (colors per GM ROI pairs were matched across the panels). Axial slices shown pass by the centroid of the VTA. (**B**) Distribution of FA values for STN in all hemispheres, and for VTA constructed with the SC at three different voltages, and for the NE contacts at entry voltage. Histogram is max-normalized to enhance the distribution of FA values. (**C**) The number of probabilistic tracts that pass by each VTA for SC at three different voltages and for NE at entry voltage. Bar graph represents the average total number of probabilistic tracts originating from the VTA to the whole-brain network for each patient at each of the shown voltage levels. For (SC) the FA distribution is similar for different VTAs (similar shape and values for 1V, entry and exit on **B**), but different number of tracts (**C**), which reflects in reaching fiber tracts towards more brain areas (**A**). On the contrary, NE contacts have a different FA distribution, more like a bimodal perhaps (**B**) have low number of total tracts (**C**), however it reaches similar target areas as the exit voltage (**A**); thus, making it noneffective even at low voltages. Average voltage values are provided in Table I. SC = stimulating contact; NE = noneffective contact.

all datasets, providing registrations that passed visual inspection and whole-brain deterministic tractography that showed full coverage of tracts and no gradient-formatting errors (Fig. 2E). For each STN case included in the study, we selected a contact as SC for each hemisphere ($N = 44$, 22 patients $\times$ 2 contacts). NE contacts were limited to $N = 7$ (5 patients) for the left hemisphere, and $N = 5$ (4 patients) for the right hemisphere. All GPi cases resulted in a pair of SC ($N = 8$, 4 patients $\times$ 2 contacts).

Validation

Anatomical validation

The individual coordinates of the selected contact and noneffective contacts were compared in the TT_N27 standard space. Left-hemisphere SCs were 2.1 ± 2.3 mm lateral, 1.9 ± 1.4 mm anterior, and 0.9 ± 2.5 mm ventral, whereas NE contacts were 0.9 ± 3.2 mm lateral, 1.4 ± 2.4 mm anterior, and 5.3 ± 2.6 mm ventral/inferior to the left STN center-of-mass. Right-hemisphere SCs were 1.7 ± 1.7 mm lateral, 1.2 ± 1.6 mm anterior, and 1.0 ± 3.0 mm dorsal, whereas NE contacts were 1.0 ± 1.9 mm lateral, 0.4 ± 2.0 mm posterior, and 3.30 ± 4.26 mm inferior to the right STN center-of-mass (Fig. 3).

Fractional anisotropy

The average FA values of voxels within the VTAs created for the SC contacts at 1 V, entry voltage and exit voltage were 0.54 ± 0.16, 0.54 ± 0.15, and 0.53 ± 0.12, respectively. A normalized histogram revealed an increasing proportion of voxels with higher FA values for the VTAs in comparison to the STN tissue (Fig. 4B). Paired t tests between FA values at the different VTA voltage levels were not statistically significant. However, the brain regions reached (Fig. 4A) and the total number of tracts passing by a particular contact's VTA increased with the increase in stimulating voltage (Fig. 4C). As described in Eq. 2), the VTA size is proportional to the stimulating voltage. Average sizes of the SCs VTA were: 4.3 ± 4.9 voxels at 1 V, 16 ± 16 voxels at entry voltage (2.0 ± 0.9 V), 55 ± 34 at exit voltage (4.3 ± 1.2 V).

The FA values of the VTAs for NE contacts and their matched SC at entry voltages were significantly different

($p = 0.01$, paired t test), being 0.51 ± 0.17 for the NE and 0.64 ± 0.20 for the SC. The normalized histogram analysis revealed a more diffuse distribution of FA values throughout NE VTA voxels compared to SC entry voltage VTA voxels (Fig. 4B).

The average FA of the STN ROIs was 0.38 ± 0.06 and increased to 0.41 ± 0.05 after inflation by two voxels, indicating the expansion into white matter tissue. Similar results were observed for the GPi ROI, where the average FA of the original ROIs was 0.28 ± 0.04, and increased to 0.34 ± 0.05 after inflation by two voxels.

Clinical voltage tractography

VTA-to-network probabilistic tracking was performed to investigate connections from three VTA estimations (at 1V and at two clinically relevant windows: entry voltage and exit voltage) for all patients at SC ($N = 44$, 22 patients × 2 contacts) and at entry voltage for the NE contacts ($N = 12$). The average voltages and radii for 1V, entry voltage, and exit voltage levels are shown in Table I. Similarly, the univariate general linear model found a main effect for voltage ($F = 22.34$, $p < 0.0001$) in this subset. Bonferroni's-corrected paired t tests between contacts with all three voltage levels ($N = 44$; 3 comparisons, $p < 0.0167$) found that SC at exit voltages had a significantly greater number of tracts than SC and entry voltages ($p < 0.0001$), and that entry voltage had a significantly greater number of tracts than 1V ($p < 0.0001$). SC and NE contacts at entry voltage were not significantly different. In most cases, voltage increases resulted in tract bundle pathways becoming denser, providing a more robust finding, or in new bundle pathways appearing, with different functional endpoint regions being affected (Fig. 4A).

DISCUSSION

Here we have described DBSproc, an open source software pipeline for combining multimodal data sets, localizing DBS electrode contacts in individual patient space, and investigating tractographic patterns of contacts at several voltage levels. Importantly, the pipeline contains both processing features (such as denoising, mapping among patient spaces, and calculating quantities of interest) and quality control steps with direct user visualization. In this work, we have presented the results of testing the proposed method using retrospective imaging data.

We have validated the proposed methodology both quantitatively and qualitatively by evaluating the locations of selected (therapeutic) contacts in relation to the STN, as defined by the AFNI Talairach–Tournoux template volume. The SCs localized dorsolateral from the NE contacts, in accordance with present targeting practices, suggest that we are localizing successfully implanted electrodes [McClelland et al., 2005; Plaha et al., 2006]. This is consistent with the positive clinical response seen in all the

TABLE I. Voltage, radii, and number of estimated tracts for each voltage level VTA

	SC 1V	SC entry	SC exit	NE entry
Voltage (V)	1.00	2.02 ± 0.86	4.25 ± 1.24	1.57 ± 0.36
Radii (mm)	1.47 ± 0.43	2.17 ± 0.69	3.36 ± 0.79	1.70 ± 0.57
Nr tracts	1.98×10^6	5.14×10^6	1.26×10^7	3.07×10^6

SC = selected contact ($N = 44$; 22 patients × 2 hemispheres), NE = noneffective contact ($N = 7$ for left hemisphere; $N = 5$ for right hemisphere).

patients included here. While the procedures were developed for the STN, we were able to apply the same procedures to a different target location (that of the GPi). Our positive findings in GPi patient data are especially encouraging, as they show that the proposed technique can be also applied to diverse DBS target populations.

Our VTAs, estimated using patient- and contact-specific voltage and impedance data, have reliably demonstrated different levels of network connectivity. These results have shown that more fibers and brain areas are reached with higher voltage/larger VTA radius; tractography measures such as the number of tracts should be interpreted with appropriate caveats and not taken to be literal representations of underlying white-matter bundles [Jones et al., 2013].

The consistency and robustness of the DBSproc method's results (demonstrated using anatomical, DTI parameter and tractographic comparisons) are due to the fact that most information is derived directly from each patient's own data. Although anatomical templates are used for tissue segmentation, the resulting tissue maps are individualized and remain within a patient-specific space. Furthermore, all image registrations rely on unique features (e.g., electrode artifacts) and our pipeline allows for quality checking in both two- and three-dimensional views.

As DBS surgical outcomes can be highly variable, these data allow us to identify overall trends of consistent regional connectivity across patients without sacrificing the ability to investigate individual structural or tractographic differences. In the current validation study, one example of this was shown using normalized tractographic statistics, which also provided a quantitative measure for the effects of voltage increases. Current work is underway to associate the local properties of the tracked WM itself (i.e., FA, mean diffusivity and other DTI parameters along the tracts) with the VTAs and DBS outcomes. Furthermore, the identification of white matter connections by grey matter targets is likely to provide better insight to physiologic, functional, and behavioral correlates [Riva-Posse et al., 2014]. This may be initially implemented by selecting electrodes and VTAs via the set of FreeSurfer parcellated GM regions that the tract bundles intersect. In future studies, however, we also plan to acquire and include resting-state or task-based fMRI data to supplement the functional outcomes.

Limitations

Our current method of estimating VTAs is limited to a simplified spherical model, which we included in the current software package due to its ability to easily incorporate patient-specific contact voltage and impedance values. Previous modeling work has incorporated the different conductivity properties of grey and white tissue as well as axonal anatomical detail [Butson et al., 2006, 2007]. The VTA estimation could therefore be improved by creating a model including tissue composition together with the clinical impedance and voltage data we are currently using.

In addition, we are unable to control for electrode localization or connectivity changes due to cell death, brain shift, or any other factors attributable the surgical implantation procedure itself. We also cannot account for variable impedance values throughout the relevant anatomic territory which impact current delivery effectiveness [Satzer et al., 2015], and how the impedance varies in time postoperatively [Cheung et al., 2014; Lungu et al., 2014].

CONCLUSIONS

Despite the limitations of the methodology, we propose a modular and open-source software pipeline (DBSproc included within the AFNI distribution) for coregistering MR and CT data for patient-specific localization and tractographic analysis of DBS electrodes. The field of DBS therapy is moving from a "target structure" approach towards a "target network" approach, and using tractography for clinical and research purposes may well become a standard approach in the near future. We expect that this pipeline will grow with further developments and refinements, including feedback from a community of users. We hope this publicly available toolbox will be used in conjunction with clinical outcome data in order to better understand the tractographic profiles or phenotypes associated with successful implantation and programming [Riva-Posse et al., 2014]. Equally important will be the network-level characterization of long-term side effects such as weight gain in STN DBS [Mills et al., 2012]. Indeed, our group has found clinically relevant tractographic differences that are beyond the scope of this manuscript. While being a research tool, we hope future results from this toolbox will inform future DBS implantation, electrode programming, and potentially aid defining new surgical targets.

ACKNOWLEDGMENTS

REFERENCES

Anthofer JM, Steib K, Fellner C, Lange M, Brawanski A, Schlaier J (2015): DTI-based deterministic fibre tracking of the medial forebrain bundle. Acta Neurochir (Wien) 157:469–477.

Basser PJ, Pierpaoli C (1996): Microstructural and physiological features of tissues elucidated by quantitative-diffusion-tensor MRI. J Magn Reson B 111:209–219.

Bazin P-L, Cuzzocreo JL, Yassa MA, Gandler W, McAuliffe MJ, Bassett SS, Pham DL (2007): Volumetric neuroimage analysis extensions for the MIPAV software package. J Neurosci Methods 165:111–121.

Butson CR, Cooper SE, Henderson JM, McIntyre CC (2007): Patient-specific analysis of the volume of tissue activated during deep brain stimulation. NeuroImage 34:661–670.

Butson CR, Maks CB, McIntyre CC (2006): Sources and effects of electrode impedance during deep brain stimulation. Clin Neurophysiol 117:447–454.

Cheung T, Noecker AM, Alterman RL, McIntyre CC, Tagliati M (2014): Defining a therapeutic target for pallidal deep brain stimulation for dystonia. Ann Neurol 76:22–30.

Cox RW (1996): AFNI: Software for analysis and visualization of functional magnetic resonance neuroimages. Comput Biomed Res 29:162–173.

Descoteaux M, Deriche R, Knösche TR, Anwander A (2009): Deterministic and probabilistic tractography based on complex fibre orientation distributions. IEEE Trans Med Imaging 28: 269–286.

Fischl B (2012): FreeSurfer. NeuroImage 62:774–781.

Gopinath RA (1998): Maximum likelihood modeling with Gaussian distributions for classification. In: Proceedings of the 1998 IEEE International Conference on Acoustics, Speech and Signal Processing, 2:661–664.

Hebb AO, Poliakov AV (2009): Imaging of deep brain stimulation leads using extended Hounsfield unit CT. Stereotact Funct Neurosurg 87:155–160.

Henderson JM (2012): "Connectomic surgery": Diffusion tensor imaging (DTI) tractography as a targeting modality for surgical modulation of neural networks. Front Integr Neurosci 6:15.

Hubble JP, Busenbark KL, Wilkinson S, Penn RD, Lyons K, Koller WC (1996): Deep brain stimulation for essential tremor. Neurology 46:1150–1153.

Hughes AJ, Daniel SE, Kilford L, Lees AJ (1992): Accuracy of clinical diagnosis of idiopathic Parkinson's disease: A clinicopathological study of 100 cases. J Neurol Neurosurg Psychiatry 55:181–184.

Jones DK, Knösche TR, Turner R (2013): White matter integrity, fiber count, and other fallacies: The do's and don'ts of diffusion MRI. NeuroImage 73:239–254.

Kovanlikaya I, Heier L, Kaplitt M (2014): Treatment of chronic pain: Diffusion tensor imaging identification of the ventroposterolateral nucleus confirmed with successful deep brain stimulation. Stereotact Funct Neurosurg 92:365–371.

Kringelbach ML, Green AL, Aziz TZ (2011): Balancing the brain: Resting state networks and deep brain stimulation. Front Integr Neurosci 5:8.

Limousin P, Krack P, Pollak P, Benazzouz A, Ardouin C, Hoffmann D, Benabid AL (1998): Electrical stimulation of the subthalamic nucleus in advanced Parkinson's disease. N Engl J Med 339:1105–1111.

Lungu C, Malone P, Wu T, Ghosh P, McElroy B, Zaghloul K, Patterson T, Hallett M, Levine Z (2014): Temporal

macrodynamics and microdynamics of the postoperative impedance at the tissue-electrode interface in deep brain stimulation patients. J Neurol Neurosurg Psychiatry 85:816–819.

Mädler B, Coenen VA (2012): Explaining clinical effects of deep brain stimulation through simplified target-specific modeling of the volume of activated tissue. Am J Neuroradiol 33: 1072–1080.

McAuliffe MJ, Lalonde FM, McGarry D, Gandler W, Csaky K, Trus BL (2001): Medical Image Processing, Analysis and Visualization in Clinical Research. In: Proceedings of the 26th IEEE International Symposium on Computer-Based Medical Systems, 0:381.

McClelland S, Ford B, Senatus PB, Winfield LM, Du YE, Pullman SL, Yu Q, Frucht SJ, McKhann GM, Goodman RR (2005): Subthalamic stimulation for Parkinson disease: Determination of electrode location necessary for clinical efficacy. Neurosurg Focus 19:E12.

Mills KA, Scherzer R, Starr PA, Ostrem JL (2012): Weight change following GPi or STN deep brain stimulation in Parkinson's disease and dystonia. Stereotact Funct Neurosurg 90:386–393.

Paek SH, Han JH, Lee J-Y, Kim C, Jeon BS, Kim DG (2008): Electrode position determined by fused images of preoperative and postoperative magnetic resonance imaging and surgical outcome after subthalamic nucleus deep brain stimulation. Neurosurgery 63:925–936 (discussion 936–937).

Pierpaoli C, Walker L, Irfanoglu MO, Barnett A, Basser P, Chang LC, Koay C, Pajevic S, Rohde G, Sarlls J, Wu M (2010): TORTOISE: An integrated software package for processing of diffusion MRI data. ISMRM 18th annual meeting, Stockholm, Sweden, 1597.

Pinsker MO, Herzog J, Falk D, Volkmann J, Deuschl G, Mehdorn M (2008): Accuracy and distortion of deep brain stimulation electrodes on postoperative MRI and CT. Zentralblatt Für Neurochir 69:144–147.

Plaha P, Ben-Shlomo Y, Patel NK, Gill SS (2006): Stimulation of the caudal zona incerta is superior to stimulation of the subthalamic nucleus in improving contralateral parkinsonism. Brain J Neurol 129:1732–1747.

Riva-Posse P, Choi KS, Holtzheimer PE, McIntyre CC, Gross RE, Chaturvedi A, Crowell AL, Garlow SJ, Rajendra JK, Mayberg HS (2014): Defining critical white matter pathways mediating successful subcallosal cingulate deep brain stimulation for treatment-resistant depression. Biol Psychiatry 76:963–969.

Rorden C, Brett M (2000): Stereotaxic display of brain lesions. Behav Neurol 12:191–200.

Saad ZS, Glen DR, Chen G, Beauchamp MS, Desai R, Cox RW (2009): A new method for improving functional-to-structural MRI alignment using local Pearson correlation. NeuroImage 44:839–848.

Saad ZS, Reynolds RC (2012): SUMA. NeuroImage 62:768–773.

Satzer D, Maurer EW, Lanctin D, Guan W, Abosch A (2015): Anatomic correlates of deep brain stimulation electrode impedance. J Neurol Neurosurg Psychiatry 86:398–403.

Schlaier J, Anthofer J, Steib K, Fellner C, Rothenfusser E, Brawanski A, Lange M (2015): Deep brain stimulation for essential tremor: Targeting the dentato-rubro-thalamic tract? Neuromodulation J Int Neuromodulation Soc 18:105–112.

Sweet JA, Walter BL, Gunalan K, Chaturvedi A, McIntyre CC, Miller JP (2014): Fiber tractography of the axonal pathways linking the basal ganglia and cerebellum in Parkinson disease: Implications for targeting in deep brain stimulation. J Neurosurg 120:988–996.

Taylor PA, Jacobson SW, van der Kouwe A, Molteno CD, Chen G, Wintermark P, Alhamud A, Jacobson JL, Meintjes EM (2015): A DTI-based tractography study of effects on brain structure associated with prenatal alcohol exposure in newborns. Hum Brain Mapp 36:170–186.

Taylor PA, Saad ZS (2013): FATCAT: (an efficient) Functional and Tractographic Connectivity Analysis Toolbox. Brain Connect 3: 523–535.

Thomas C, Ye FQ, Irfanoglu MO, Modi P, Saleem KS, Leopold DA, Pierpaoli C (2014): Anatomical accuracy of brain connections derived from diffusion MRI tractography is inherently limited. Proc Natl Acad Sci USA 111:16574–16579.

Vidailhet M, Vercueil L, Houeto J-L, Krystkowiak P, Benabid A-L, Cornu P, Lagrange C, Tézenas du Montcel S, Dormont D, Grand S, Blond S, Detante O, Pillon B, Ardouin C, Agid Y, Destée A Pollak P, French Stimulation du Pallidum Interne dans la Dystonie (SPIDY) Study Group (2005): Bilateral deep-brain stimulation of the globus pallidus in primary generalized dystonia. N Engl J Med 352:459–467.

Volkmann J, Moro E, Pahwa R (2006): Basic algorithms for the programming of deep brain stimulation in Parkinson's disease. Mov Disord 21 Suppl 14:S284–S289.

Wells WM, Viola P, Atsumi H, Nakajima S, Kikinis R (1996): Multi-modal volume registration by maximization of mutual information. Med Image Anal 1:35–51.